


FULL PAPER

Open Access



Ground strains induced by the 2022 Hunga-Tonga volcanic eruption, observed by a 1500-m laser strainmeter at Kamioka, Japan

Akiteru Takamori^{1*} , Akito Araya¹, Kouseki Miyo², Tatsuki Washimi³, Takaaki Yokozawa², Hideaki Hayakawa² and Masatake Ohashi⁴

Abstract

In this study, we detected the horizontal ground strains induced by the atmospheric Lamb wave emitted from the 2022 eruption of the Tonga–Hunga Ha’apai undersea volcano, at an underground observatory in Kamioka, Japan. The observed strains were in the range of 10^{-11} – 10^{-10} and were measured precisely using a 1500-m laser strainmeter with a high resolution in the order of 10^{-12} . This was one of the first observations of a Lamb wave using a laser strainmeter. The strainmeter was constructed in a tunnel of the KAGRA gravitational-wave telescope. Our observations demonstrate that strain and atmospheric pressure were clearly correlated, resulting in a regression coefficient of $-(2.3 - 3.7) \times 10^{-10}$ strain/hPa. This finding was compared with the responses under regular pressure conditions and the estimations obtained using the local deformation and traveling wave models. The observed coefficients for the Lamb wave exhibited smaller magnitudes than those observed under regular conditions and take values between that of the two theoretical models. These results reflect the intermediate scale of the pressure distribution of the Lamb wave between the assumptions of the simple models. The strain variations were also found to have started earlier than the corresponding pressure changes at the observation site with characteristic time lags ranging from 25 to 155 s. In addition, several aspects related to the mechanism that created the time lags are discussed.

Keywords Strainmeter, Strain, Atmospheric pressure, Tonga–Hunga 2022, Lamb wave, KAGRA, Kamioka

*Correspondence:

Akiteru Takamori

takamori@eri.u-tokyo.ac.jp

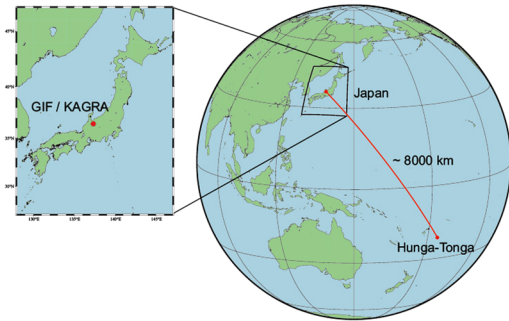
Full list of author information is available at the end of the article



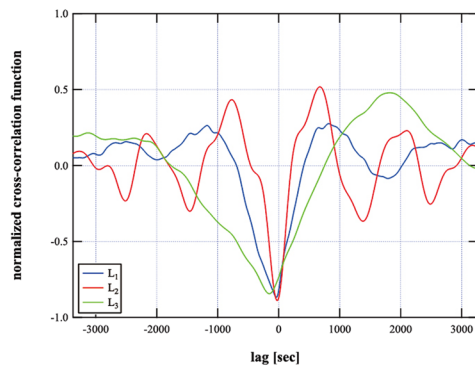
© The Author(s) 2023. **Open Access** This article is licensed under a Creative Commons Attribution 4.0 International License, which permits use, sharing, adaptation, distribution and reproduction in any medium or format, as long as you give appropriate credit to the original author(s) and the source, provide a link to the Creative Commons licence, and indicate if changes were made. The images or other third party material in this article are included in the article's Creative Commons licence, unless indicated otherwise in a credit line to the material. If material is not included in the article's Creative Commons licence and your intended use is not permitted by statutory regulation or exceeds the permitted use, you will need to obtain permission directly from the copyright holder. To view a copy of this licence, visit <http://creativecommons.org/licenses/by/4.0/>.

Graphical Abstract

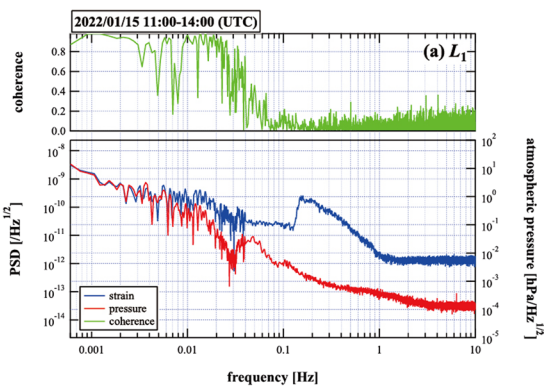
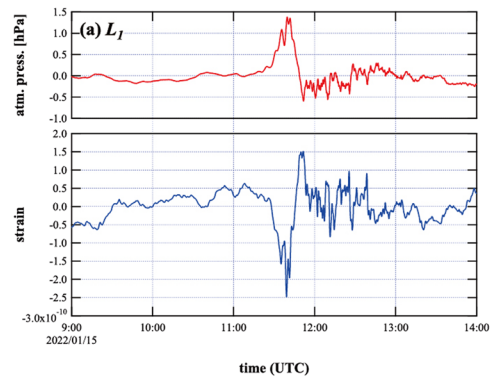
Ground strains induced by the 2022 Hunga-Tonga volcanic eruption, observed by a 1500-m laser strainmeter in Kamioka, Japan



Locations of Hunga-Tonga volcano and Kamioka



Cross-correlation functions between air-pressure and strain indicate time lags between them



Atmospheric pressure and horizontal strain of the first Lamb wave (L_1): waveforms (top) and spectra (bottom)

Introduction

The large eruption of the Tonga–Hunga Ha’apai under-sea volcano which occurred at 04:14 on January 15, 2022 UTC produced various phenomena, e.g., seismic and acoustic disturbances, tsunamis, and ionospheric disturbances on a global scale (Matoza et al. 2022; Carvajal et al. 2022; Zhang et al. 2022). One of the most remarkable phenomena was the Lamb wave, which was detected as fluctuations of atmospheric pressure at numerous observation sites while circling the Earth for a few days after this historic volcanic event occurred. In addition, for the first time, horizontal deformations induced by the Lamb wave were observed using laser strainmeters by us and at another observatory (Dolgikha et al. 2022).

Atmospheric loading induces deformations of the Earth and occasionally hinders geodetic and seismological measurements by introducing noises in the signals of instruments, e.g., seismometers, tiltmeters, strainmeters, and gravimeters (Zürn et al. 2007, 2015; Imanishi 2022). The effect of atmospheric pressure on ground deformations is a classical problem, and several models based on theory of elasticity have been proposed to resolve this problem (Sorrels 1971; Farrell 1972). However, these models often disagree with the observation results (Steffen et al. 2005; Mouyen et al. 2017), which indicates that there is a lack of clarity regarding our general understanding of pressure-induced ground strain. This may suggest that various factors are not considered in these simple models, e.g., topographic effects, meteorological

effects, or the dynamic response of the crustal structure, and these omitted factors may introduce measurable discrepancies between the observations and the simple models. Thus, extensive corresponding studies have been conducted, including numerical modeling based on the finite element method and the analysis of seasonal variation of strain response to pressure (Mentes and Eper-Pápai 2009; Kroner et al. 2005; Steffen et al. 2005; Gebauer et al. 2010). In addition, previous studies have estimated that atmospheric loading in the vicinity of the observation point (and in the wider area) appears to cause nonnegligible effects on ground deformations (Akutsu et al. 2021). This introduces another complexity to the evaluations of loading effect because it is generally difficult to detect the exact distribution of air pressure over a wide region. In this context, the Lamb wave emitted from the undersea volcano provided a unique opportunity to better understand the mechanism of the loading effect because it created a distribution of air pressure that can be estimated with little uncertainty, virtually forming a coherent plane wave at remote locations, e.g., Japan, which is distant from the wave's origin point. This particular condition should resolve the complexity related to the uncertainty of atmospheric pressure distribution under normal conditions and allowed us to evaluate the spatial range within which the air loading induced the deformations at the strainmeter location.

The Lamb wave generated by the eruption of the undersea volcano in Tonga was observed using a 1500-m laser strainmeter at the Kamioka Observatory, which has a resolution in the order of 10^{-12} , and this is the best

resolution at the frequencies of interest (1 mHz to 10 Hz; Araya et al. 2017). This excellent signal-to-noise ratio allowed us to investigate the relationships between pressure and strain precisely by analyzing their waveforms and spectra.

In this paper, following a brief description of the Kamioka Observatory in the next section, we report the observation results of atmospheric pressure changes caused by the Lamb wave, and the horizontal strains induced by these changes. The results of the observations are then discussed and compared with theoretical models.

The 1500-m laser strainmeter at Kamioka Observatory

In 2016, we constructed a laser strainmeter in the underground site of the gravitational-wave antenna KAGRA (Kamioka, Gifu Prefecture, Japan). This site comprises two orthogonally excavated tunnels measuring 3 km in length (Akutsu et al. 2020). The laser strainmeter with a 1500-m baseline length is referred to as the Geophysics Interferometer (GIF) and is still in operation in the KAGRA's "X-arm" tunnel (Araya et al. 2017). The locations of the GIF and KAGRA are shown in Fig. 1. The GIF is located at 36.416° N latitude, 137.316° E longitude, 377 m a.s.l., approximately 380 m below the surface (these values are for the midpoint of the instrument based on the digital elevation model supplied by The Geospatial Information Authority of Japan) with an azimuth of $N 61.7^\circ$ E, horizontal (Brady et al. 2021). The location and

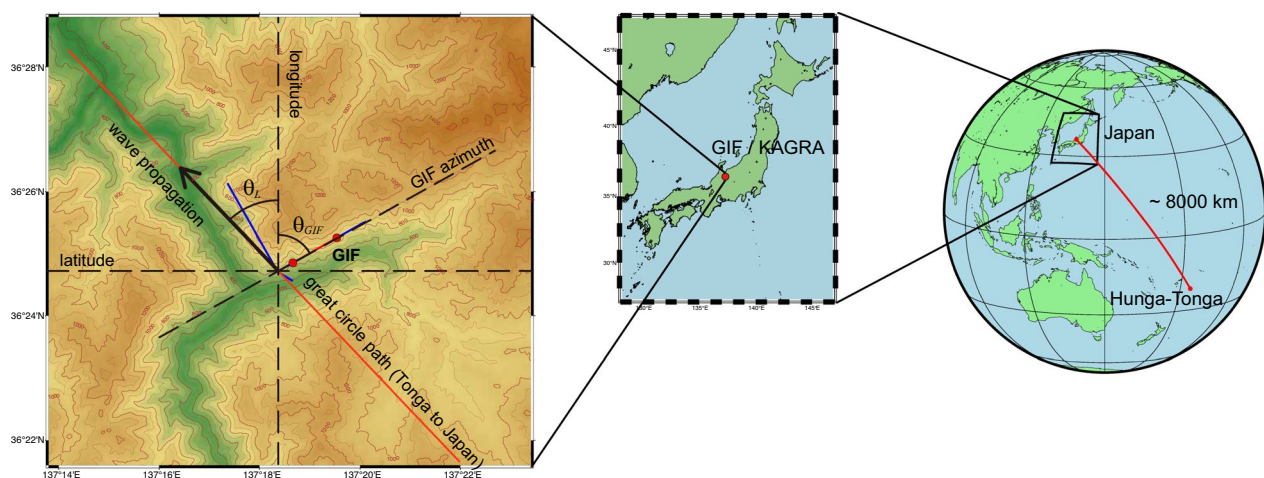


Fig. 1 Right and center: locations of the 1500-m laser strainmeter (GIF) at the KAGRA site and the Hunga-Tonga undersea volcano, respectively. The red curve represents the Great circle path between the KAGRA site and the volcano, along which the Lamb wave emitted by the eruption is supposed to have traveled to Japan, thereby forming a plane-wave-like pressure distribution. Left: topographical map around the KAGRA site in Kamioka. The GIF (red circles) is installed in one of the KAGRA tunnels (blue). The Great circle path is shown by the red line running SE to NW. A fraction of the strain induced by the traveling wave was observed as the GIF is rotated by approximately 105° from the propagation path

orientation of the tunnel were determined to obtain a large cover depth of soil to reduce seismic noise for KAGRA. The GIF was designed and installed for geophysical observations and was expected to provide valuable information about the tunnel deformation for KAGRA to enable active baseline compensations (Akutsu et al. 2021; Miyo 2020). It is essentially a Michelson laser interferometer equipped with unequal arm lengths (Fig. 2), and the displacement of the main 1500-m baseline is measured using the quadrature phase detection technique and a high-frequency-stabilized laser that realizes a linear strain resolution better than 10^{-11} within the frequency range studied in this paper (Agnew 1986; Araya et al. 2002). The front end of the GIF (X500) is located approximately 960 m (path length) from the entrance of the KAGRA tunnel behind nonairtight steel doors, and its other end (X2000) is 1500 m from X500. The GIF covers wide frequency and spatial ranges. It regularly observes the tidal strains with amplitudes of the order of 10^{-8} and microseisms where the amplitude strongly relates to the weather condition of the Sea of Japan (in the range of 10^{-11} to 10^{-10} around 200 mHz), as well as regional earthquakes that induces large strain fluctuations of the order of 10^{-7} without saturating (Akutsu et al. 2018; Araya et al. 2017). In theory, the GIF can record horizontal linear strains continuously as long as the interferometric phase is tracked; however, it is occasionally interrupted by human activities in the tunnel (for the commissioning work of KAGRA) and other practical issues such as power outages.

To monitor atmospheric pressure at the GIF, Vaisala PTB110 barometric pressure sensors are deployed at both X500 and X2000. The recorded pressure at both of these ends was virtually identical with the pressure recorded outside the tunnel (Washimi et al. 2022), which was likely due to the loose closure of the tunnel by the steel doors described earlier.

Observations and data processing

Waveforms and cross-correlation analysis

Here, 24-bit analog-to-digital converters were used to record the output fringe signals of the GIF and the signals of barometric pressure sensors at sampling rates of 50 kHz and 200 Hz, respectively. The fringe signals were then converted to an interferometric phase representing the displacements of the 1500-m arm and resampled at 20 Hz. The average linear strain along the interferometer baseline was obtained by dividing the displacements by the nominal baseline length of 1500 m. Note that the tidal strains contribute the largest to the strain amplitude. Theoretical tidal strains, including solid Earth and oceanic tidal loading, were calculated using the GOTIC2 software, and then subtracted from the observed strain data to investigate the effect of atmospheric loading (Matsumoto et al. 2001). The theoretical strain was synthesized by a linear combination of three horizontal strain components because the strain at the Kamioka site is influenced by topographical effects. Here, the combination coefficients, i.e., α , β , and γ , were determined by minimizing the sum of errors from the observed tidal strain as follows:

$$S(\varepsilon) = \sum \{\varepsilon_{\text{obs}} - (\alpha\varepsilon_{\text{NS}} + \beta\varepsilon_{\text{EW}} + \gamma\varepsilon_{\text{SH}})\}^2, \quad (1)$$

where ε_{obs} denotes the observed strain, ε_{NS} , ε_{EW} , and ε_{SH} denote the theoretical linear strains in the north–south direction, the east–west direction, and the shear strain, respectively. Each combination of weighting factors was determined using the strain data with a period of 24 h, including the corresponding arrival of the Lamb wave. An example of the strain data preprocessing is illustrated in Fig. 3. High-frequency noises were removed by applying a second-order Butterworth low-pass filter with a cutoff frequency of 0.01 Hz to the detided strain and atmospheric pressure data. Note that only the pressure data recorded at X500 are considered in this paper because the atmospheric pressure changes at the two

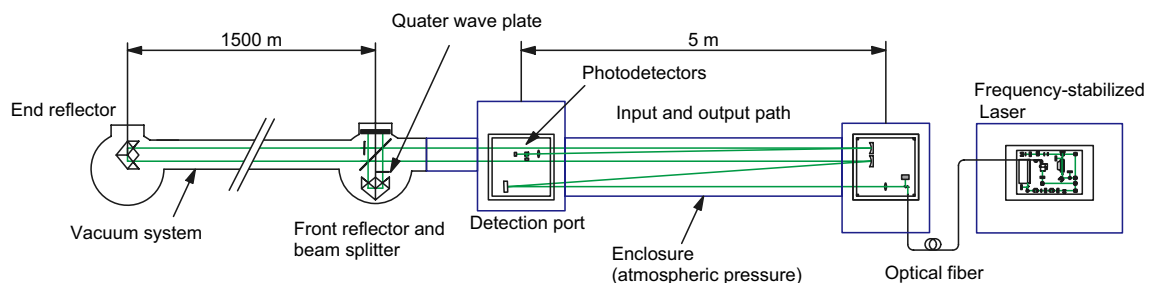


Fig. 2 Diagram of GIF adopted from the literature (Araya et al. 2017) with minor modifications. A frequency-stabilized laser beam is introduced to an input mode matching telescope to locate the beam waist at the position of the end reflector, and a quarter wave plate is inserted in the reference arm to enable the quadrature phase detection

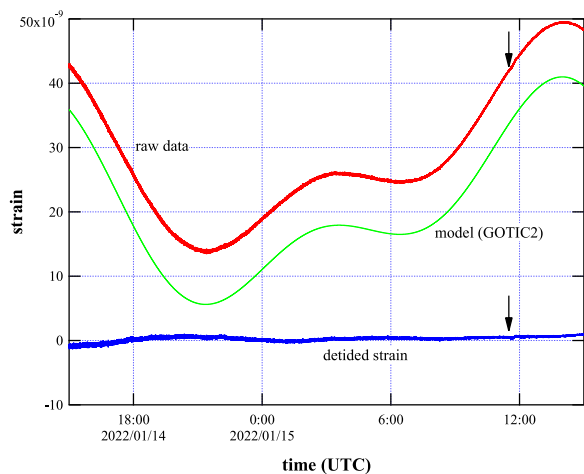


Fig. 3 Strain data preparation process. The theoretical tide (compression negative) was calculated using GOTIC2 and weighted (green) to best reproduce the raw observed strain (red). Their difference gives a detided strain (blue). Arbitrary offset is added to each curve for clarity. The arrows indicate a tiny glitch associated with the arrival time of the first Lamb wave (L_1)

ends of the GIF were observed to be identical (Akutsu et al. 2021).

Figure 4a shows the detided strain observed by the GIF at the arrival of the first Lamb wave (L_1) that traveled along the minor arc from the south to arrive at approximately 11:30 UTC, i.e., 7 h and 15 min after the eruption. A clear negative correlation between the pressure and strain can be seen immediately. The maximum variations of the atmospheric pressure and strain were approximately 1.9 hPa and -4.0×10^{-10} , respectively, where the negative sign means compression. A normalized cross-correlation function was calculated as follows in consideration of the slight offset in time (time lag) between the strain and pressure:

$$R_{\varepsilon,p}(n) = \begin{cases} \sum_{m=0}^{N-n-1} \frac{\varepsilon(n+m)p(m)}{\sqrt{R_{\varepsilon}R_p}} & , n \geq 0, \\ \sum_{m=0}^{N+n-1} \frac{\varepsilon(m)p(-n+m)}{\sqrt{R_{\varepsilon}R_p}} & , n < 0, \end{cases} \quad (2)$$

$$R_{\varepsilon} = \sum_{m=1}^N \varepsilon(m)^2, \quad R_p = \sum_{m=1}^N p(m)^2, \quad (3)$$

where ε and p denote the detrended strain and pressure samples, respectively, N denotes the number of samples and $\tau = \Delta t \times n$ gives the time lag between the strain and pressure (Δt is the sampling interval). The shape and peak values of the cross-correlation function were found to be strongly dependent on the period of data used in

the calculation. Thus, to evaluate the effect of the Lamb wave as efficiently as possible, we carefully selected data periods that satisfied the following criteria: (1) each period must contain the main (significant) peak(s) of the Lamb wave, and (2) the absolute value of the largest negative peak of $R_{\varepsilon,p}$ must be greater than 0.8, i.e., a strong negative correlation between the pressure and strain is required. The periods of data used in the calculations are listed in Table 1. For L_1 , the strongest correlation ($|R_{\varepsilon,p}| \sim 0.87$) occurred at approximately -40.4 s of time lag, which indicates that the strain changed ahead of the pressure. To evaluate the uncertainty of the time lag, a full width of the negative peak at which the amplitude of the peak decreases by 10% was calculated (Table 1). As can be seen, for L_1 , it is 156 s.

In Table 1, from left to right: the indexes of the Lamb wave; periods of data used to calculate the cross-correlation functions and transfer functions between the strain and atmospheric pressure; minimum values of the cross-correlation functions (equivalent to the strongest negative correlation coefficients); and the corresponding time lags and full width at which the correlation decreases by 10% from the peaks. The negative lags indicate the strain changes ahead of the pressure. The regression coefficients obtained from the mean magnitude of the transfer functions in 0.6–3 mHz are given in the rightmost column.

Figure 4b and c shows the waveforms for the second (L_2) and third (L_3) waves, which arrived from the north and south together with their corresponding strains. As shown, the maximum amplitudes of pressure for L_2 were 0.43 hPa, and that for L_3 was 1.1 hPa. Note that the pressure variations for L_2 were substantially less than those for other waves. The cross-correlation functions for L_2 and L_3 were computed in the same manner as for L_1 . The results are plotted in Fig. 5. As shown in Table 1, the strongest correlations and the corresponding time lags were negative in all cases, which indicates that the changes in strain occurred prior to the local pressure variations.

Frequency domain analysis

Figure 6a–c shows the spectra of the strain and atmospheric pressure fluctuations along with their coherences for $L_1 - L_3$, respectively, and the periods of data used to compute the spectra are listed in Table 1 (second column). The strain fluctuation induced by the microseisms appears as a broad peak around 0.2 Hz. Note that the spectra of the strain and pressure have similar shapes below 3 mHz in all cases, and their high coherences, which indicate their strong correlations, are observed at these frequencies. A high coherence associated with the resonance of the tunnel at 28 mHz was observed in 10–30 mHz range for L_1 (Washimi

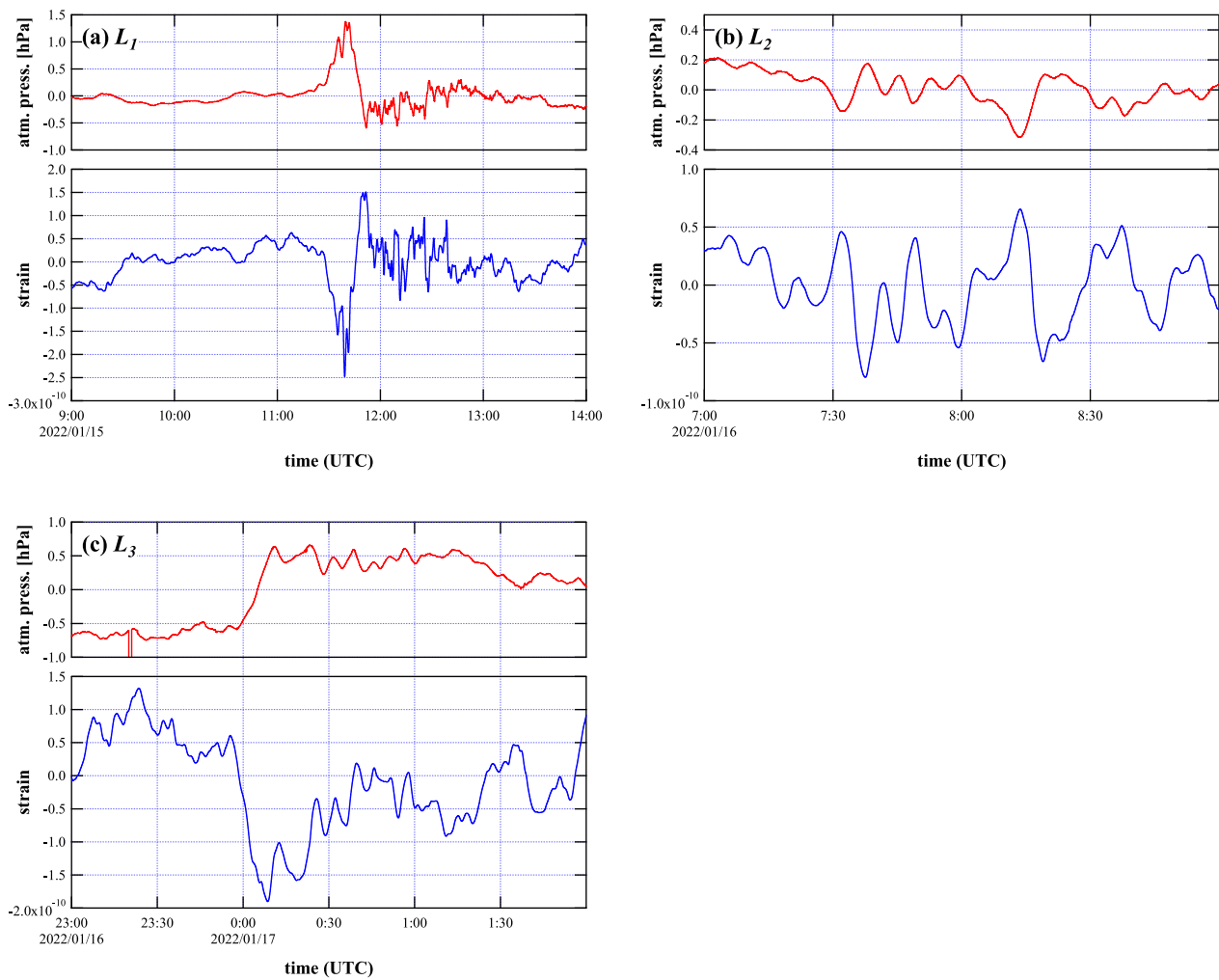


Fig. 4 Detided strain (blue, compression negative) and atmospheric pressure (red) variations observed at the arrival of the first direct Lamb wave **a** L_1 , the second wave **b** L_2 , and the third wave **c** L_3 . Linear trends were removed from the detided strain shown in Fig. 3 and from the pressure data prior to applying a 0.01 Hz low-pass filter. The visibility of L_2 may be lower than others and insignificant relative to the background fluctuations; however, its arrival was confirmed by a similar waveform recorded at a distant observatory (see Appendix)

Table 1 Summary of data analysis

Lamb wave	Period (UTC)	Best correlation coefficient	Corresponding lag [second]	Full width (10% decrease) [second]	Regression coefficient [strain/hPa]
L_1	2022/1/15 11:20–13:00	− 0.87	− 40.4	156	$− 2.4 \times 10^{-10}$
L_2	2022/1/16 07:30–09:00	− 0.89	− 25.1	113	$− 3.7 \times 10^{-10}$
L_3	2022/1/16 23:30–2022/1/17 01:30	− 0.84	− 155	273	$− 2.6 \times 10^{-10}$

et al. 2022). The transfer functions between the strain and pressure were computed using the same dataset to investigate the regression coefficients between them. The results are shown in Fig. 7a–c for $L_1 - L_3$, respectively. As can be seen, the magnitudes and phases of the transfer functions become nearly flat and close to

−180°, respectively, in the frequency band where higher coherences were observed. This observation is consistent with the negative correlations seen in the time-domain data. The mean values of magnitude in 0.6 – 3 mHz were calculated to obtain the regression coefficients, and the results are summarized in Table 1. Note

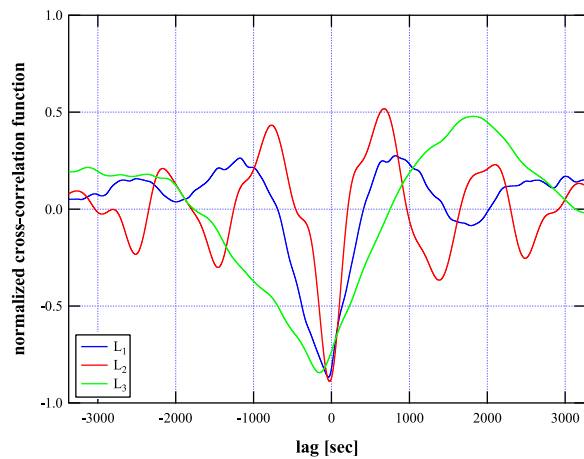


Fig. 5 Cross-correlation functions computed between the observed strain and atmospheric pressure fluctuations for L_1 (blue), L_2 (red), and L_3 (green). The strongest negative correlation corresponds to a time lag between strain and pressure. The dispersed waveform and the influence of background noise may have caused multiple peaks with same levels of amplitude for L_2 . These were computed from the records in the periods given in Table 1

that the scales of the left (strain) axes in Fig. 6a–c are adjusted by multiplying the range of the right (pressure) axes by these coefficients, which allows us to visually confirm that the strain and pressure spectra coincide below a few mHz.

Discussion

Response to regular pressure fluctuations

The response of ground deformation to regular fluctuations of atmospheric pressure was calculated as a reference because the Lamb wave from the eruption was an unusual event. Note that the term “regular fluctuations” refers to moderate meteorological conditions that exclude harsh changes in pressure, e.g., typhoons. Five time periods of 12-h stretch, in which the correlations between strain and pressure were observed in waveforms, were selected by considering the weather conditions and avoiding earthquakes or human activities in the tunnel for commissioning the KAGRA telescope, which introduce noises to the laser strainmeter (refer to Fig. 10 for an example). Using the same procedure described in the previous section, the spectra of the strain and pressure were computed using the 12-h data (Fig. 11). The regression coefficients were obtained by calculating the mean values of the flat part of their ratio (strain/pressure) at the low frequencies, which is equivalent to the magnitude of a transfer function, depicting high coherence ($\gtrsim 0.8$), as shown in Fig. 8 and summarized in Table 2. These analyses were performed using the data acquired within three weeks before and one week after

the eruption, and the resulting coefficients agree within 11%. Although a coefficient with a larger magnitude, i.e., -5.5×10^{-10} strain/hPa, was reported by Akutsu et al. (2021), it was obtained from the ratio of the spectra of the strain and pressure recorded in October 2017, i.e., more than four years prior to the occurrence of the eruption of the Tonga–Hunga Ha’apai volcano. Thus, the coefficient for regular pressure fluctuations during the arrivals of the Lamb wave can be assumed to be close to those obtained in the closer days in Table 2 with an average of $\xi_{\text{GIF,reg}} = -4.7 \times 10^{-10}$ strain/hPa.

The theoretical strain caused by atmospheric pressure over an elastic half-space is given as follows:

$$\Delta \varepsilon_{\text{iso}} = -\frac{1}{4\mu} \left(\frac{\mu}{\lambda + \mu} \right) P \equiv \xi_{\text{iso}} P, \quad (4)$$

$$\xi_{\text{iso}} = -4.3 \times 10^{-10} [\text{strain/hPa}], \quad (5)$$

where P denotes the pressure, and λ and μ refer to the Lamé parameters according to the general results of the surface strain presented by Farrell (1972, p. 769). In this model, the ground is assumed to be isotropically deformed by the local pressure. The Lamé parameters of the local bedrock were determined using a blasting experiment, where $\lambda = 32.7$ GPa and $\mu = 25.1$ GPa (Takemoto et al. 2003). We found that the regression coefficient observed under regular conditions $\xi_{\text{GIF,reg}}$ was consistent with the theoretical value of ξ_{iso} within 10%. Thus, the local deformation model is considered to be an effective representation of the regular spatial pressure conditions.

Discussion on the response to Lamb wave

Using the observations from the GIF, the regression coefficients of the horizontal ground strain in response to the atmospheric pressure fluctuations created by the Lamb wave were obtained as $\xi_{\text{GIF,obs}} = -(2.3 - 3.7) \times 10^{-10}$ strain/hPa. The coefficients for L_1 and L_3 were in agreement within 12%, and their absolute values were less than that of L_2 . Note that the L_2 coefficient might be overestimated because the pressure variation created by the Lamb wave was not as significant as that of L_1 and L_3 relative to the background pressure fluctuations; thus, the effect of the background fluctuation may have caused nonnegligible influences. The observed coefficients have smaller absolute values compared to those of the response of the GIF to regular pressure variations. However, it is unlikely caused by the temporal variations of coefficient due to seasonal or meteorological conditions (Mentes and Eper-Pápai 2009) because the coefficient for regular fluctuations was supposed to be stable during the arrival of Lamb wave as discussed in the previous subsection.

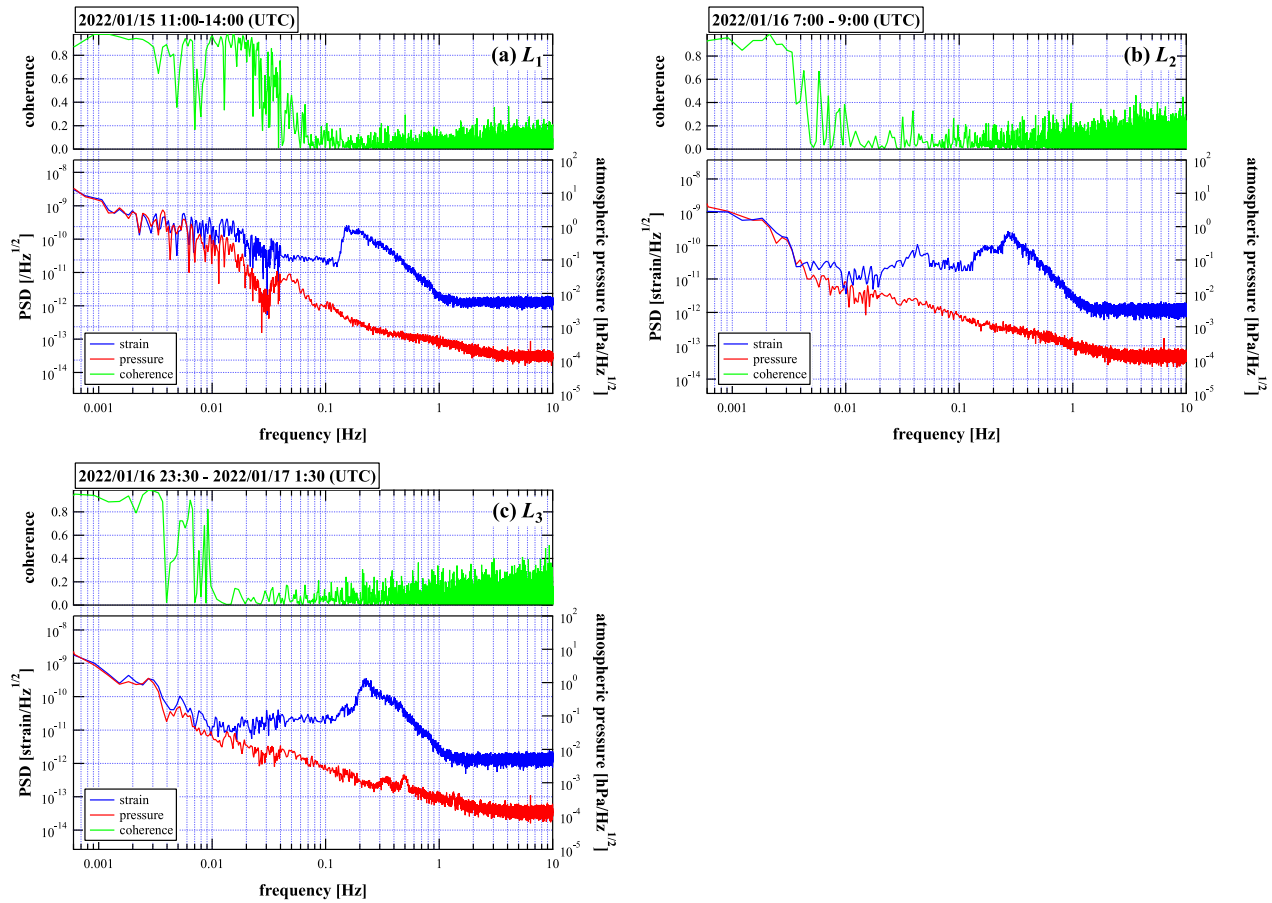


Fig. 6 Spectra of detided strain and atmospheric pressure fluctuations for **a** L_1 , **b** L_2 , and **c** L_3 (plotted with coherence). The higher coherences and similarity in the shapes of the strain and pressure spectra were commonly observed below a few mHz, which suggests a strong correlation between them, as expected from the waveforms shown in Fig. 4

To better understand this discrepancy, we consider the “Traveling wave model (TWM)” discussed by Zürn et al. (2007). The pressure disturbances created by the Lamb wave traveled as a distinct unidirectional plane wave, while the usual meteorological phenomena generated relatively slow pressure fluctuations with more complicated spatial distributions in a greater area. This observation satisfies the conditions of the TWM. According to the TWM (Eq. 10 in Zürn et al. 2007), the horizontal strains induced on the ground surface by atmospheric pressure that propagate as a plane wave along the x axis is given as follows:

$$\Delta \varepsilon_{xx, \text{TWM}} = -\frac{1}{2\mu} \left(\frac{\mu}{\lambda + \mu} \right) P \equiv \xi_{\text{TWM}} P. \quad (6)$$

Note that the plane wave induces the horizontal strain only in the propagation direction ($\Delta \varepsilon_{yy, \text{TWM}} = 0$, y is orthogonal to x). Thus, the theoretical strain observable by the GIF is expected to be:

$$\xi_{\text{GIF, TWM}} = \xi_{\text{TWM}} \cos^2 \Delta \theta, \quad (7)$$

$$\Delta \theta = \theta_L + \theta_{\text{GIF}}, \quad (8)$$

where θ_L and θ_{GIF} denote the direction of propagation and the azimuth of the GIF, respectively. In our case $\theta_L = \text{N}43.60^\circ \text{W}$, considering the Great circle path from the undersea volcano to Kamioka based on GRS80. The geometric relations of the propagation path and the azimuth of the GIF are illustrated in Fig. 1 (left). The theoretical regression coefficient was calculated as $\xi_{\text{GIF, TWM}} = -6.0 \times 10^{-11}$ strain/hPa using Eqs. (6), (7) (8). This value is much less than the observed value of $\xi_{\text{GIF, obs}}$ by a factor of 3.8–6.2 (in absolute values). This difference is too large to be caused by the deviation of propagation path from the great circle or distortion of the wave front from an ideal plane wave that could be caused by strong winds; nevertheless westerly windy conditions were observed at the time of arrival (Watada et al.

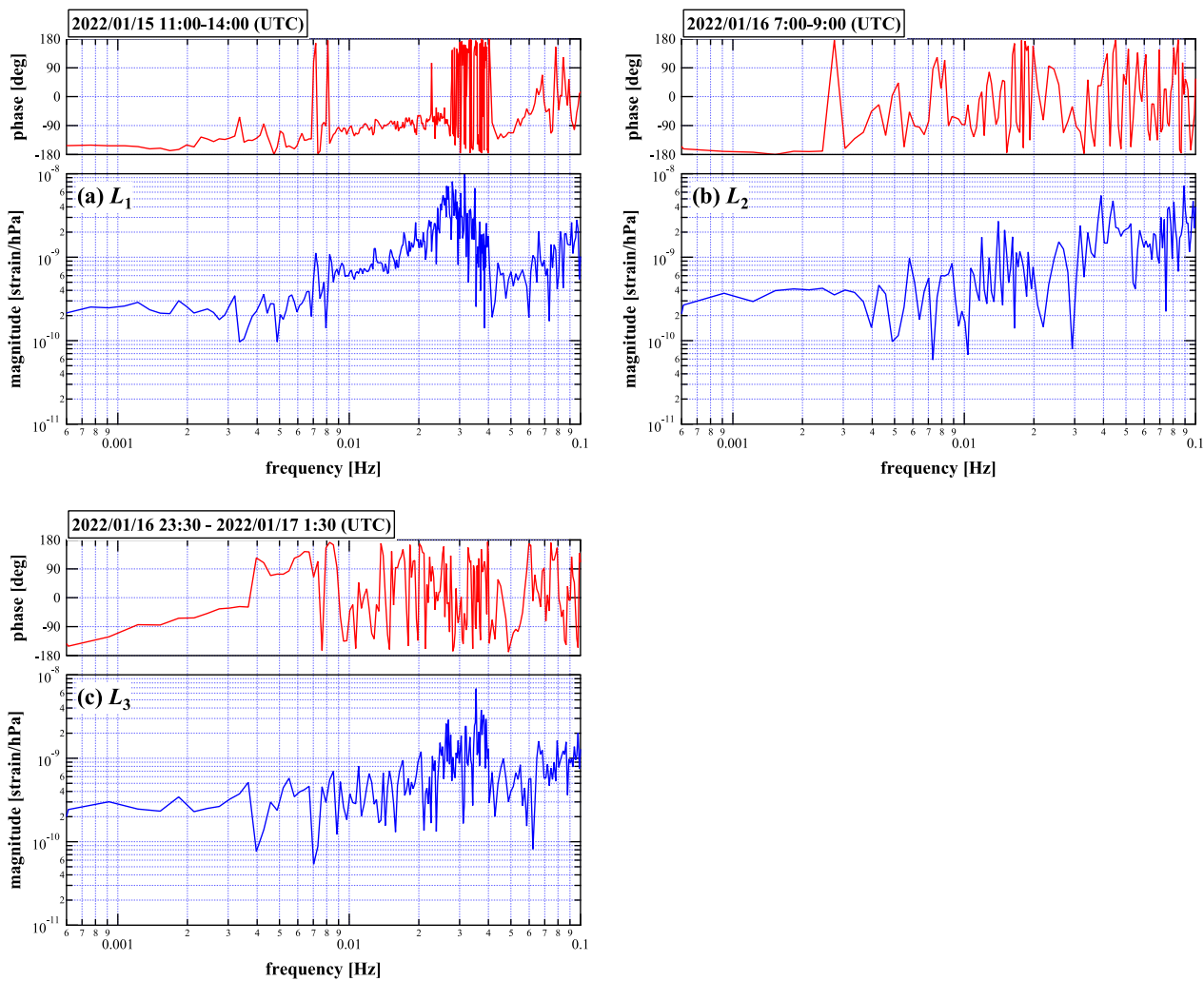


Fig. 7 Bode plots of transfer functions from the atmospheric pressure to horizontal strain calculated for (a) L_1 , (b) L_2 , and (c) L_3 using the data recorded in the periods shown in Table 1. The peak around 30–40 mHz corresponds to the resonance of the tunnel (Washimi et al. 2022)

2023). In case the discrepancy resulted solely from the redirection of the propagation path, it must be rotated to the east by greater than 45 degrees, which, in the current

Table 2 Regression coefficients between strain and atmospheric pressure in regular conditions obtained from the mean values of spectra ratio at low frequencies (Fig. 6)

Date (JST, UTC +9)	Regression coefficient [strain/hPa]
2021/12/25 00:00–2021/12/25 12:00	-4.7×10^{-10}
2021/12/26 00:00–2021/12/26 12:00	-4.8×10^{-10}
2022/1/1 12:00–2022/1/2 00:00	-4.3×10^{-10}
2022/1/22 15:00–2022/1/23 03:00	-4.9×10^{-10}
2022/1/23 12:00–2022/1/24 00:00	-4.6×10^{-10}
Average	-4.7×10^{-10}

scenario, seems impossible. The reduction in the coefficient could be attributed to the peculiar timescale and spatial distribution of the atmospheric pressure carried by the Lamb wave. This can be interpreted as an intermediate state between the wide pressure distribution assumed in the local deformation model and the linear load distribution on which the TWM is based. This may result in a regression coefficient that lies between the expected values from these ideal models. The observed width of the main peak pressure of the Lamb wave was 1000–2000s, which corresponds to a width of 310–620 km in space. Here, it is assumed that the typical group velocity of Lamb waves is 310 m/s (Matoza et al. 2022). This is sufficiently large relative to the characteristic range where atmospheric loading causes strains. Thus, it seems reasonable that the response of the ground deformation became closer to that of the isotropic

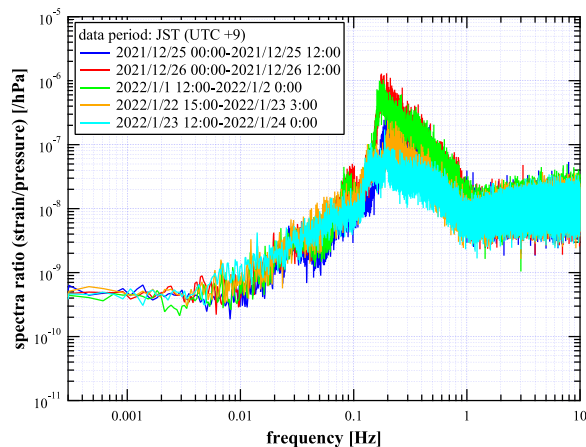


Fig. 8 Ratio of strain and atmospheric pressure spectra under regular meteorological conditions, before and after the eruption. A dataset with a 12-h period was used to calculate each these ratios. The regression coefficients were obtained by calculating the mean values at frequencies less than 3 mHz where high ($\gtrsim 0.8$) coherence was obtained between the strain and pressure

pressure rather than the local pressure at the point of strain observation carried by a plane wave, which is considered in the TWM [Eq. (6)].

As shown in Table 1, the characteristic time lag between the strain variations and pressure changes was found to be 25.1–155 s, and the strain was found to change ahead of pressure in all events. The strain-before-pressure sequences were also observed in the records used to calculate the response under regular conditions at the GIF and have been reported for other sites (Onoue 1993; Kroner et al. 2005). The time lags reported by Onoue and Kroner were in the order of hours and identified after several days of observations, and those for the Lamb wave were in the order of 10–100 s. This may indicate a positive correlation between the time scale of the atmospheric pressure changes and the time lags. First, we assumed that the time lags were created by the regional loading effect, as implicated by Akutsu et al. (2021), using the data under general conditions, i.e., the Lamb wave induced the measurable strain at the GIF site when the wave front was still distant. However, if this is the case, the same effect should occur after the wave passed the site, and it should have caused a broadened strain peak and a zero-centered peak of each cross-correlation function. However, these after effects were not observed. This finding may suggest the need for some factors not included in the models based on a static response of a half-space with linear elasticity to a surface loading, to understand the response of crustal deformations to atmospheric loadings. Such factors may include dynamic coupling

between crustal deformations and atmosphere, the effect of the curvature of the Earth, and topographic effects (Canitano 2020). It was demonstrated by finite element modeling that topographic effects can cause complicated ground deformation when a high pressure area passes over a strainmeter (Gebauer et al. 2010). Note, this is an untested hypothesis; however, it was postulated only after the clear observation of the strains induced by the Lamb wave.

Conclusions

In this paper, we have presented clear observations about the horizontal ground strains with the 1500-m laser strainmeter GIF at Kamioka, Japan, induced by the atmospheric pressure fluctuations caused by the Lamb wave emitted from the eruption of the Tonga–Hunga Ha’apai undersea volcano, which occurred January 15, 2022. Given the high resolution of the instrument, the horizontal linear strain variations were accurately observed to be in the range of 10^{-11} to 10^{-10} . The waveforms exhibited an apparent negative correlation between strain and pressure, and this correlation was confirmed by the high coherence between them below a few mHz. Using the low-frequency component of the transfer functions between strain and pressure, the regression coefficients were determined to be $-(2.3 - 3.7) \times 10^{-10}$ strain/hPa. In addition, the regression coefficient to regular pressure fluctuations was calculated using the data observed before and after the eruption, which turned out to be stable during the events with an average of -4.7×10^{-10} strain/hPa. Thus, the response to the Lamb wave was significantly smaller in magnitude compared to that of the regular pressure variations. The regression coefficients for the Lamb wave obtained in this study were also compared with two theoretical models, i.e., the local deformation model, which represents the regular pressure condition, and the TWM, which assumes a pressure distribution corresponding to a traveling plane wave front while rejecting deformations orthogonal to a propagation path. The observation result was intermediate between the estimates obtained using these models. This may reflect the medium spatial scale of the Lamb wave between the extreme situations assumed in these simple models. The time lag between the strain variations and pressure fluctuations was found to lie between 25 and 155 s (i.e., the strain changed ahead of pressure), which was not expected from the static model describing the effect of the surface loading on an elastic half-space. However, further observations under various conditions are required to better understand the origin of the time lag and improve the theoretical models.

Appendix

Identification of Lamb wave

To determine the periods of data used in the analysis of each Lamb wave, the atmospheric pressure fluctuations measured at distant observatories were compared with those of the GIF. We found that the waveforms were highly site dependent, and were affected by local wind and air temperature variations. However, similar waveforms were found at some observatories at the expected time of arrival, and these were used to identify L_1 – L_3 . The atmospheric pressure fluctuations observed at the GIF and Kirishima Volcano Observatory (KVO) of the Earthquake Research Institute of the University of Tokyo are shown in Fig. 9 as an example. The identifications of L_1 and L_3 were obvious; however, that of L_2 was somewhat difficult because it had relatively small amplitude, which was also distorted by the local atmospheric disturbances. By carefully comparing two waveforms, some notable peaks were found to correspond,

which are indicated by the green arrows in Fig. 9, to help us identify L_2 .

Strain and atmospheric pressure with a longer time-window

The response of horizontal strain to the air pressure under regular conditions was calculated using 12-h data. The time-series data for one of these periods, i.e., during 2021/12/26 00:00–12:00 (JST, UTC + 9), are shown in Fig. 10. The strain variations also led the atmospheric pressure in this time scale. Figure 11 shows the spectra of the strain and air pressure of the data shown in Fig. 10 together with the coherence and ratio between them. Here, the regression coefficient was calculated from the mean value of the ratio in 0.8–3 mHz, where a high coherence (> 0.8) was observed.

See Figs. 9, 10, 11

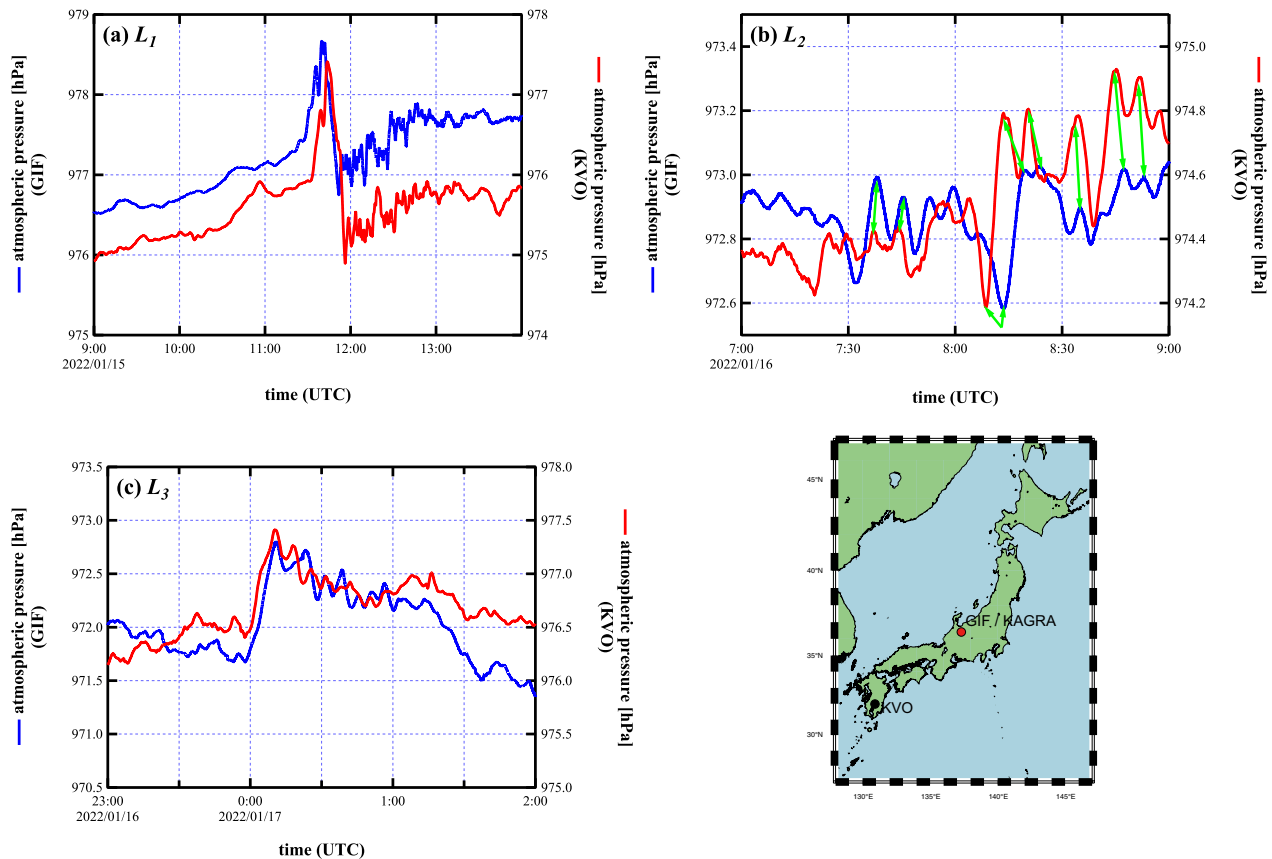


Fig. 9 Atmospheric pressure observed at GIF and KVO. Similar waveforms were observed at these distant sites (the corresponding locations are shown in the map at the bottom-right). L_1 (a) and L_3 (c) arrived at KVO after the GIF, and L_2 (b) was detected at KVO before the GIF. Some corresponding peaks in L_2 are indicated by green arrows

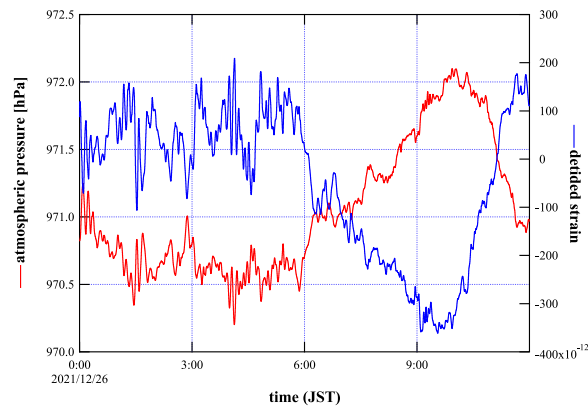


Fig. 10 The dedided strain and atmospheric pressure observed in 2021/12/26 00:00–12:00 (JST). These data were used to calculate the response of the horizontal strain to a regular pressure variation (Table 2)

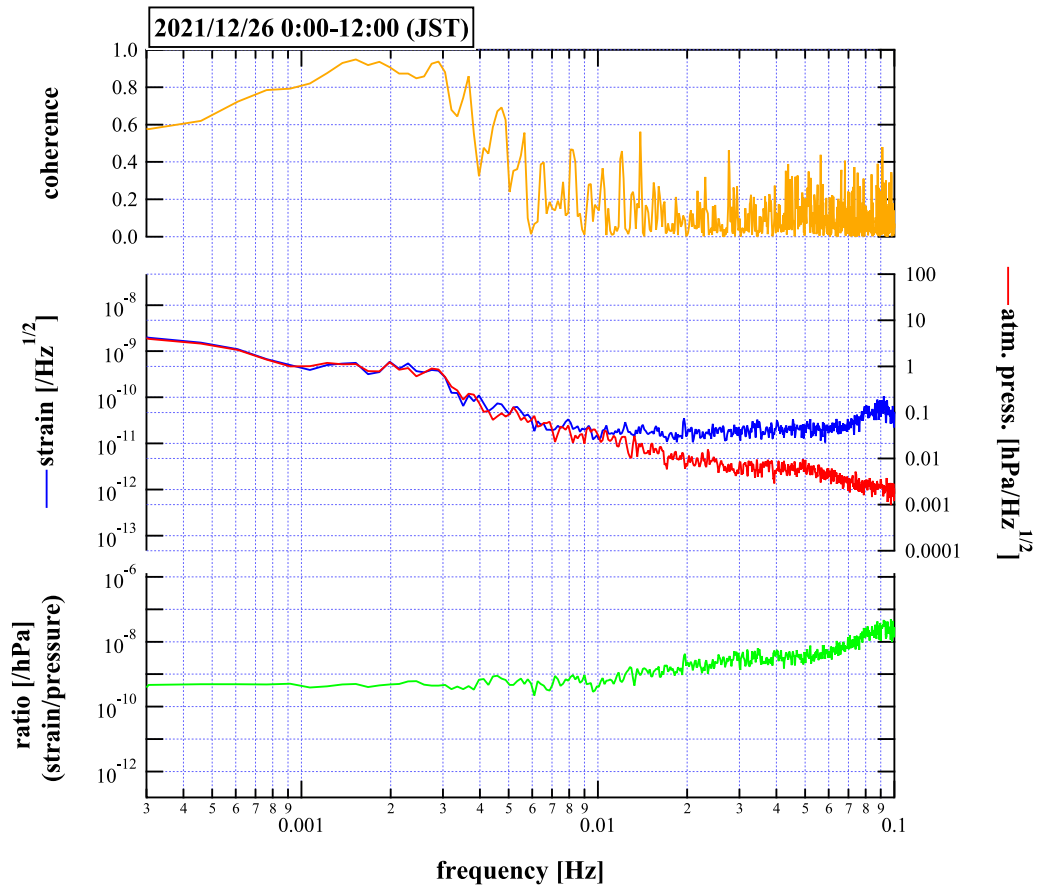


Fig. 11 The spectra (middle) of the data plotted in Fig. 10. The coherence (top) and ratio (bottom) between the strain and pressure are also shown

Acknowledgements

The authors would like to express gratitude to Wataru Morii for developing a data acquisition system for GIF. We also would like to express gratitude to the KAGRA collaborators and the facility staff who supported our work. Records of atmospheric pressure provided by the Volcano Research Center of Earthquake Research Institute, University of Tokyo, helped the authors determine the arrival times of the Lamb wave. This work was supported by Ministry of Education, Culture, Sports, Science and Technology (MEXT), Japan Society for the Promotion of Science (JSPS) in Japan; National Research Foundation (NRF) and Ministry of Science and ICT (MSIT) in Korea; Academia Sinica (AS) and National Science and Technology Council (NSTC) in Taiwan. This research is also supported by the Institute for Cosmic Ray Research Inter-University Research Programs (2006–2022). We wish to thank Wataru Morii, who designed and built the data acquisition system for GIF, and the KAGRA collaborators and facility staff who supported our work.

Author contributions

AT designed, installed and maintained the laser strainmeter, managed the research schedule, and analyzed the data. AA designed the interferometer and vacuum system, provided the data analysis tool, and managed the overall research. KM designed the data acquisition system and maintained the laser strainmeter. TW provided information about the KAGRA environment monitoring system. TY managed the KAGRA environment monitoring system. HH maintained the laser strainmeter and data acquisition system. MO managed site infrastructure, and supervised the whole project.

Funding

This work was supported by the Ministry of Education, Culture, Sports, Science and Technology (MEXT), Japan Society for the Promotion of Science (JSPS) in Japan; the National Research Foundation (NRF) and Ministry of Science and ICT (MSIT) in Korea; Academia Sinica (AS) and the National Science and Technology Council (NSTC) in Taiwan. This research was also supported by the Institute for Cosmic Ray Research Inter-University Research Programs (2006–2022).

Availability of data and materials

The data used in this paper are not publicly available for a limited time period, following the data policy of KAGRA.

Declarations

Competing interests

Not applicable.

Author details

¹Earthquake Research Institute, University of Tokyo, 1-1-1 Yayoi, Bunkyo-ku, Tokyo 113-0032, Japan. ²Institute for Cosmic Ray Research, KAGRA Observatory, The University of Tokyo, 238 Higashi Mozumi, Kamioka-cho, Hida City, Gifu 506-1205, Japan. ³Kamioka Branch, National Astronomical Observatory of Japan (NAOJ), 238 Higashi Mozumi, Kamioka-cho, Hida City, Gifu 506-1205, Japan. ⁴Institute for Cosmic Ray Research, The University of Tokyo, 5-1-5, Kashiwanoha, Kashiwa, Chiba 277-8582, Japan.

Received: 15 February 2023 Accepted: 6 June 2023

Published online: 16 June 2023

References

- Agnew DC (1986) Strainmeters and tiltmeters. *Rev Geophys* 24:579–624
- Akutsu T et al (2018) Construction of KAGRA: an underground gravitational-wave observatory. *Prog Theor Exp Phys*. <https://doi.org/10.1093/ptep/ptx180>
- Akutsu T et al (2020) Overview of KAGRA: detector design and construction history. *Prog Theor Exp Phys*. <https://doi.org/10.1093/ptep/ptaa125>
- Akutsu T et al (2021) Overview of KAGRA: calibration, detector characterization, physical environmental monitors, and the geophysics interferometer. *Prog Theor Exp Phys*. <https://doi.org/10.1093/ptep/ptab018>
- Araya A, Kunigi T, Fukao Y, Ymada I, Suda N, Maruyama S, Mio N, Moriwaki S (2002) Iodine-stabilized Nd:YAG laser applied to a long-baseline interferometer for wideband earth strain observations. *Rev Sci Instrum* 73:2434–2439
- Araya A, Takamori A, Morii W, Miyo K, Ohashi M, Hayama K, Uchiyama T, Miyoki S, Saito Y (2017) Design and operation of a 1500-m laser strainmeter installed at an underground site in Kamioka, Japan. *Earth Planets Space* 69:77. <https://doi.org/10.1186/s40623-017-0660-0>
- Brady P, Losurdo G, Shinkai H (2021) LIGO, VIRGO, and KAGRA as the International Gravitational Wave Network. In: Bambi C et al (eds) *Handbook of gravitational wave astronomy*. Springer, Singapore. https://doi.org/10.1007/978-981-15-4702-7_51-1
- Canitano A (2020) Observation and theory of strain-infrasound coupling during ground-coupled infrasound generated by Rayleigh waves in the longitudinal valley (Taiwan). *Bull Seismol Soc Am* 110(6):2991–3003. <https://doi.org/10.1785/0120200154>
- Carvajal M, Sepúlveda I, Gubler A, Garreaud R (2022) Worldwide signature of the 2022 Tonga Volcanic Tsunami. *Geophys Res Lett* 49:e2022GL098153. <https://doi.org/10.1029/2022GL098153>
- Dolgikha GI, Dolgikha SG, Ovcharenko VV (2022) Atmospheric and deformation disturbances caused by the Hunga-Tonga-Hunga-Ha'apai Volcano. *Dokl Earth Sci* 505(2):575–577. <https://doi.org/10.1134/S1028334X22080074>
- Farrell WE (1972) Deformation of the earth by surface loads. *Rev Geophys Space Phys* 10:761–797
- Gebauer A, Steffen H, Kroner C, Jahr T (2010) Finite element modelling of atmosphere loading effects on strain, tilt and displacement at multi-sensor stations. *Geophys J Int* 181:1593–1612. <https://doi.org/10.1111/j.1365-246X.2010.04549.x>
- Imanishi Y (2022) Inertial effects due to eruption-induced atmospheric disturbances identified by superconducting gravimeter observations at Matsushiro, Japan. *Earth Planets Space* 74:54. <https://doi.org/10.1186/s40623-022-01615-4>
- Kroner C, Jahr Th, Kuhlmann S, Fischer KD (2005) Pressure-induced noise on horizontal seismometer and strainmeter records evaluated by finite element modelling. *Geophys J Int* 161:167–178
- Matoza RS et al (2022) Atmospheric waves and global seismoacoustic observations of the January 2022 Hunga eruption, Tonga. *Science* 377(6601):95–100. <https://doi.org/10.1126/science.abo7063>
- Matsumoto K, Sato T, Takanezawa T, Ooe M (2001) GOTIC2: a program for computation of oceanic tidal loading effect. *J Geod Soc Jpn* 47(1):243–248
- Mentes G, Eper-Pápai I (2009) Relations between microbarograph and strain data. *J Geodyn* 48:110–114. <https://doi.org/10.1016/j.jog.2009.09.005>
- Miyo, K. (2020) A Study of Baseline Compensation System for Stable Operation of Gravitational-wave Telescopes. PhD Thesis, University of Tokyo.
- Mouyen M, Canitano A, Chao BF, Hsu Y-J, Steer P, Longuevergne L, Boy J-P (2017) Typhoon-Induced Ground Deformation. *Geophys Res Lett* 44(21):11004–11011. <https://doi.org/10.1002/2017GL075615>
- Onoue K (1993) Effects of atmospheric pressure on ground strains observed at Donzuruboo observatory. *Annu Disas Prev Res Inst Kyoto Univ* 36B-1:365–372
- Sorrells GG (1971) A preliminary investigation into the relationship between long-period seismic noise and local fluctuations in the atmospheric pressure field. *Geophys J R Astr Soc* 26:71–82
- Steffen H, Kuhlmann S, Jahr T, Kroner C (2005) Numerical modelling of the barometric pressure-induced noise in horizontal components for the observatories Moxa and Schiltach. *J Geodyn* 41:242–252. <https://doi.org/10.1016/j.jog.2005.08.011>
- Takemoto S et al (2003) Installation of 100m laser strainmeters in the Kamioka Mine. *Annu Disas Prev Res Inst Kyoto Univ* 46:749–755
- Washimi T, Yokozawa T, Takamori A, Araya A, Hoshino S, Itoh Y, Kobayashi Y, Kume J, Miyo K, Ohkawa M, Oshino S, Tomaru T, Yokoyama J, Yuzurihara H (2022) Response of the underground environment of the KAGRA observatory against the air pressure disturbance from the Tonga volcanic eruption on January 15, 2022. *Prog Theor Exp Phys*. <https://doi.org/10.1093/ptep/ptac128>
- Watada S, Imanishi Y, Tanaka K (2023) Detection of air temperature and wind changes synchronized with the lamb wave from the 2022 tonga volcanic eruption. *Geophys Res Lett* 50:e2022GL100884. <https://doi.org/10.1029/2022GL100884>
- Zhang S-R, Vierinen J, Aa E, Goncharenko LP, Erickson PJ, Rideout W, Coster AJ, Spicher A (2022) 2022 Tonga volcanic eruption induced global

propagation of ionospheric disturbances via Lamb waves. *Front Astron Space Sci* 9:871275. <https://doi.org/10.3389/fspas.2022.871275>

Zürn W, Exß J, Steffen H, Kroner C, Jahr T, Westerhaus M (2007) On reduction of long-period horizontal seismic noise using local barometric pressure. *Geophys J Int* 171:780–796. <https://doi.org/10.1111/j.1365-246X.2007.03553.x>

Zürn W, Ferreira AMG, Widmer-Schmid R, Lentas K, Rivera L, Clévéde E (2015) High-quality lowest-frequency normal mode strain observations at the Black Forest Observatory (SW-Germany) and comparison with horizontal broad-band seismometer data and synthetics. *Geophys J Int* 203:1787–1803. <https://doi.org/10.1093/gji/ggv381>

Publisher's Note

Springer Nature remains neutral with regard to jurisdictional claims in published maps and institutional affiliations.

Submit your manuscript to a SpringerOpen[®] journal and benefit from:

- ▶ Convenient online submission
- ▶ Rigorous peer review
- ▶ Open access: articles freely available online
- ▶ High visibility within the field
- ▶ Retaining the copyright to your article

Submit your next manuscript at ▶ [springeropen.com](https://www.springeropen.com)
